Journal of Non-Newtonian Fluid Mechanics 259 (2018) 1–15

Contents lists available at ScienceDirect

Journal of Non-Newtonian Fluid Mechanics

journal homepage: www.elsevier.com/locate/jnnfm

3D numerical simulation of free-surface Bingham fluids interacting with structures using the PFEM

Alessandro Franci [a,b,*], Xue Zhang [a,c]

[a] International Center for Numerical Methods in Engineering (CIMNE), Spain
[b] Universitat Politècnica de Catalunya (UPC) Gran Capitán s/n, Campus Norte UPC, Barcelona 08034, Spain
[c] Department of Civil Engineering and Industrial Design, University of Liverpool, Liverpool, United Kingdom

A B S T R A C T

This paper presents a purely Lagrangian approach for the 3D simulation of Bingham free-surface fluids and their interaction with deformable solid structures. In the proposed numerical strategy, the fluid is handled using the Particle Finite Element Method (PFEM) to tackle the issues resulting from extreme changes of geometry, such as mesh distortion and free-surface evolution. Additionally, the Papanastasiou model is employed as a regularization technique to overcome the computational difficulties associated with the classical Bingham model. The solid structure, on the other hand, is represented by the hypoelastic constitutive model and simulated using the conventional Finite Element Method (FEM). The coupling between the fluid and the structure is achieved via a monolithic approach, called Unified formulation. Several numerical examples are presented to illustrate the correctness and the robustness of the proposed formulation, in 2D and in 3D. Special attention is devoted to the analysis of the convergence behavior of the proposed computational framework, the effect of the regularization on the numerical results and the 3D effects. Moreover, detailed comparisons between the simulated results and experimental data are performed so that the concerned problems and results can serve as benchmarks.

1. Introduction

This work presents a three-dimensional (3D) numerical method for the simulation of free-surface Bingham fluids and their interaction with elastic structures.

The Bingham model [8] is one of the most studied and used non-Newtonian law [2]. It has so-far been applied to the simulation of a wide range of engineering problems, such as debris flows [42,57,68], landslides [16,61], snow avalanches [9,18], mud flows [36,39] and fresh cement slump tests [14]. The attractiveness of the Bingham model lies in its simplicity and generality. Indeed, the Bingham material behaves like a solid under a threshold stress value, whereas, when the yield stress is exceeded, it starts to flow as a fluid. Owing to this feature, the Bingham model is very popular for simulating fluid solutions with solid/rigid particle suspension. Nevertheless, the single-phase approximation of multi-phase materials is reasonable only under certain conditions, for example when a macroscopic phase segregation is not produced [30,34,53]. From the computational point of view, the main drawbacks of the Bingham law are associated with its piecewise relation between the deviatoric stress and the strain rate, and the indeterminate value of stress under the yield stress limit. Notably, the use of the more general Herschel-Bulkley model [25] does not help to avoid this computational difficulty. For this reason, a regularized Bingham model has strategies proposed by Bercovier and Engelman [7] and Papanastasiou [52]. The Papanastasiou model succeeds in regularizing the Bingham model with good accuracy, when appropriate values of the regularization parameter are used. Although the method suffers from some numerical inconveniences (*e.g.* the ill-conditioning of the linear system [62] and the incapability of reproducing the quiescent state when the fluid is at rest [45]), the Papanastasiou model is still one of the most used regularization methods, due to the easiness of its implementation in fluid dynamic solvers. The Papanastasiou model has been applied to a wide range of engineering problems successfully, *e.g.* in [1,14,43,44,64]. These considerations have motivated the use of this regularized method in the present study.

In particular, the Papanastasiou model has been implemented into a three-dimensional (3D) Particle Finite Element Method (PFEM) framework for free-surface fluid dynamics [49]. The numerical simulation of a free-surface fluid is complex because of the continuous evolution of its boundaries. In case of using an Eulerian solving strategy, this must be complemented by a specific technique capable of tracking the fluid free-surface at each analysis step, such as Level Set method [9] or Volume Of Fluid (VOF) [37]. On the contrary, Lagrangian strategies, computing at the material points and updating continuously their positions, detect automatically the free-surface of the fluid. Nevertheless, a Lagrangian mesh cannot solve large deformation processes [72] be-

e are three possible ways approach [18,21,56], the biviscous model [18], and the regularization e use of a computational mesh, to use an hybrid Eulerian/Lagrangian strategy, or to remesh.

* Corresponding author.
E-mail address: falessandro@cimne.upc.edu (A. Franci).

https://doi.org/10.1016/j.jnnfm.2018.05.001
Received 29 January 2018; Received in revised form 27 March 2018; Accepted 2 May 2018
Available online 3 May 2018

The Smoothed-Particle Hydrodynamics (SPH) [38] belongs to the first category. See [26,40,54,63] for the application of this mesh-less method to landslides and mud flows simulations. On the other hand, both the Material Point Method (MPM) [66] and the PFEM2 [4] fit in the second class. These approaches use an Eulerian fixed mesh for computation, while a cloud of Largangian particles allows for tracking the deforming computational domain. For applications of the MPM and PFEM2 to landslide simulations refer to [3,55] and [5], respectively. Finally, the PFEM [50] adopts the latter strategy, that is to regenerate completely the mesh when it reaches a prearranged threshold of distortion. The PFEM has been already applied in the past for the simulation of natural hazards involving geophysical free-surface fluids, see for example [15,32].

The PFEM is based on an efficient remeshing strategy, which allows to dispose a good finite element mesh throughout the duration of the computation, even when highly deforming bodies are involved. In addition, the PFEM remeshing strategy allows to detect the contact between fluid and solid domains. This is of paramount importance for solving fluid-structure interaction (FSI) problems. In this work, the FSI solution is obtained through a monolithic strategy, called Unified formulation [23]. The method is derived by the original algorithm presented in [28]. The main idea of the Unified formulation is to compute fluids and solids according to the same Updated Lagrangian Velocity-Pressure implicit solver. However, while the fluid parts of the domain are remeshed with the PFEM, the structural parts maintain the same mesh for all the duration of the analysis and are solved with the standard Finite Element Method (FEM). This is done to avoid the introduction of interpolation errors into the solid historical variables computation.

To the best of the authors' knowledge, in the literature there are very few solvers for non-Newtonian free-surface fluids interacting with deformable structures, and even less are those capable of tackling 3D geometries. In [33], the Lattice–Boltzmann Method (LBM) [65] is used to simulate the impact of geophysical flows against rigid walls. An hybrid Discrete Element Method (DEM)-LBM-FEM has been employed in [35] to reproduce the debris flow impact over a flexible and permeable barrier. A similar problem has been analyzed in [46] with an Arbitrary Lagrangian-Eulerian (ALE) formulation and the finite element software LS-DYNA. Finally, in [31] and [17] the impact of a debris flow over a ring net metallic barrier and highly stiff elastic obstacles, respectively, has been studied numerically. This general lack of numerical formulations is accompanied by an even more poor literature of experimental tests analyzing the impact of non-Newtonian fluids over deformable barriers.

This work aims to fill the vacuum in this important field, by presenting a robust and accurate numerical framework for computing the interaction between Bingham free-surface fluids and elastic structures, and by proposing some easy-to-reproduce numerical tests for benchmarking 2D and 3D FSI solvers applied to the same field. In order to show the applicability of the formulation to real engineering problems, the numerical examples have been solved considering the actual 3D geometries of the laboratory tests. The numerical analyses include the simulation of two fresh concrete slump tests, the study of a bentonite solution flow over an inclined plane with/without the impact of a falling object, and a series of dam break against an highly deformable structure analyzed for different values of the yield stress. The numerical results have been compared to those obtained either by laboratory tests or by other numerical formulations. The numerical examples are also used to test several crucial issues of the computational method, such as the mesh and the non-linear convergence and the effect of the stabilization parameter on the numerical results. A special attention has been deserved to the analysis of the 3D effects and to the validity of the plane strain assumption.

The structure of the article is the following. Section 2 is dedicated to the governing equations of the problem and the used constitutive laws. Then, in Section 3 the essential features of the PFEM are recalled and in Section 4 the FSI solution scheme is described. Section 5 is devoted to the numerical simulations and their validation. Finally, in Section 6 the conclusions of the work are summarized.

2. Governing equations

The governing equations of the problem consist of the balance of linear momentum and the mass conservation. Considering an Updated Lagrangian framework, these equations read respectively as

$$\rho\dot{\boldsymbol{v}} - \nabla\cdot\boldsymbol{\sigma} - \boldsymbol{b} = \boldsymbol{0} \qquad \text{in } \Omega\times(0,t) \tag{1}$$

$$\frac{1}{\kappa}\dot{p} - \nabla\cdot\boldsymbol{v} = 0 \qquad \text{in } \Omega\times(0,t) \tag{2}$$

where ρ is the density of the material, $\boldsymbol{v}$ is the velocity vector, $\boldsymbol{\sigma}$ is the Cauchy stress tensor, $\boldsymbol{b}$ is the body force per unit of volume, κ is the material bulk modulus and p is the pressure. Finally, Ω denotes the updated/deformed computational domain, and t is the time. Note that the pressure is defined as positive in tensile state.

The mass balance equation (Eq. (2)) is here solved in the quasi-incompressible form, as originally proposed in [28,60]. In order to recover the standard Navier-Stokes problem, an infinite material bulk modulus should be considered, resulting in the fully-incompressible form of the mass balance equation ($\nabla\cdot\boldsymbol{v}=0$).

The governing equations are complemented by the following boundary conditions

$$\begin{aligned} v_i - v_i^p &= 0 \qquad \text{on } \Gamma_v \\ \sigma_{ij}n_j - t_i^p &= 0 \qquad \text{on } \Gamma_t \end{aligned} \tag{3}$$

where v_i^p and t_i^p are the velocities and tractions prescribed at the Dirichlet (Γ_v) and Neumann (Γ_t) boundaries, respectively, and $\boldsymbol{n}$ is the normal vector.

2.1. Constitutive laws

For incompressible materials, it is useful to split the Cauchy stress tensor into its deviatoric and volumetric parts as follows

$$\boldsymbol{\sigma} = \boldsymbol{\tau} + p\boldsymbol{1} \tag{4}$$

where $\boldsymbol{\tau}$ is the deviatoric part and $\boldsymbol{1}$ is the second order identity tensor.

For a steady unidimensional shear, the deviatoric stress of a Bingham fluid is defined as

$$\begin{aligned} \tau_{xy} &= \tau_0 + \mu\frac{\partial v_x}{\partial y} \qquad \text{for } \left|\tau_{xy}\right| \geq \tau_0 \\ \frac{\partial v_x}{\partial y} &= 0 \qquad \text{for } \left|\tau_{xy}\right| < \tau_0 \end{aligned} \tag{5}$$

where τ_0 is the shear yield stress and μ is the dynamic viscosity.

In this work, a regularized Bingham law, namely the Papanastasiou model [52], is used in order to overcome the computational difficulties arisen by the non-smooth law described in Eq.(5). According to the Papanastasiou 3D model, the deviatoric stresses are computed as

$$\boldsymbol{\tau} = 2\left[\mu + \frac{\tau_0}{|\dot{\gamma}|}\left(1 - e^{-m|\dot{\gamma}|}\right)\right]\boldsymbol{d} \tag{6}$$

where m is the regularization parameter, $\boldsymbol{d}$ is the deformation rate tensor defined as

$$\boldsymbol{d} = \frac{1}{2}\left(\nabla\boldsymbol{v} + (\nabla\boldsymbol{v})^T\right) \tag{7}$$

and $|\dot{\gamma}|$ is the equivalent strain rate computed from the deformation rate tensor $\boldsymbol{d}$ as

$$|\dot{\gamma}| = (2\boldsymbol{d} : \boldsymbol{d})^{\frac{1}{2}} \tag{8}$$

From a comparison between Eqs. (5) and (6), it arises that the Papanastasiou model, unlike the Bingham law, is not capable of reproducing the rigid behavior. As a consequence, the fluid flow, although it can reach

an almost static state, it cannot stop completely. However, the fluid may reach such small velocities that it can be considered at rest from an engineering perspective, as it will be shown in Section 5. In this sense, the regularization parameter has a key role for the approximation of the Bingham curve for small values of the shear strain rate. As it is shown in Fig. 1, the higher is m, the better is the approximation of the rigid behavior of the original Bingham model. The effect of the regularization parameter on the numerical results will be analyzed and shown in a couple of problems studied in Section 5. Note that m has the dimension of the time. However, for simplicity, in the following the dimension of m will be omitted.

It is remarkable that the Papanastasiou regularized law can describe both Newtonian and non-Newtonian behaviors. For example, the Newtonian law ($\boldsymbol{\sigma} = 2\mu\boldsymbol{d} + p\mathbf{1}$) is obtained if a null shear yield stress is considered in Eq. (6).

For the solid parts of the computational domain, an hypoelastic law is used. Considering the Jaumann measure, the rate of the Cauchy stress tensor $\boldsymbol{\sigma}^{\nabla}$ is computed from the deformation rate tensor as [6]

$$\boldsymbol{\sigma}^{\nabla} = \boldsymbol{c}^{\nabla J} : \boldsymbol{d} \tag{9}$$

where the fourth-order tensor $\boldsymbol{c}^{\nabla J}$ is the Jaumann tangent moduli which, for an isotropic material, is defined as

$$\boldsymbol{c}^{\nabla J} = \kappa \mathbf{1} \otimes \mathbf{1} + 2\, G\mathbf{I}' \tag{10}$$

where G is the shear modulus and $\mathbf{I}'$ is a fourth-order tensor computed as

$$\mathbf{I}' = \mathbf{I} - \frac{1}{3}\mathbf{1} \otimes \mathbf{1} \tag{11}$$

with $\mathbf{I}$ being the fourth-order symmetric identity tensor.

The rate of Cauchy stress $\boldsymbol{\sigma}^{\nabla}$ is then integrated in time according to the scheme described in [24] to obtain the Cauchy stress of the solid.

2.2. Discretized problem

The governing equations of the problem, Eqs. (1) and (2), are discretized in the standard finite element fashion. Applying a Galerkin isoparametric discretization of the four nodal unknowns of the problem, *i.e.* three components of nodal velocities $\bar{\boldsymbol{v}}$ and the nodal pressure $\bar{p}$, the semi-discretized form of Eqs. (1) and (2) at the time instant t^{n+1} reads

$$\boldsymbol{M}_{\rho}\dot{\bar{\boldsymbol{v}}}^{n+1} + \boldsymbol{K}\bar{\boldsymbol{v}}^{n+1} - \boldsymbol{F}^{n+1} = \mathbf{0} \tag{12}$$

$$\boldsymbol{M}_{\kappa}\dot{\bar{\boldsymbol{p}}}^{n+1} - \boldsymbol{Q}\bar{\boldsymbol{v}}^{n+1} = \mathbf{0} \tag{13}$$

where $\boldsymbol{M}_{\rho}$ is the mass matrix, $\boldsymbol{K}$ is the stiffness-type matrix that contains the constitutive information, and $\boldsymbol{F}$ is the external force vector. The matrix $\boldsymbol{M}_{\kappa}$ has the same structure as $\boldsymbol{M}_{\rho}$ however it depends on the bulk modulus rather than the density, and $\boldsymbol{Q}$ is the discretized divergence operator.

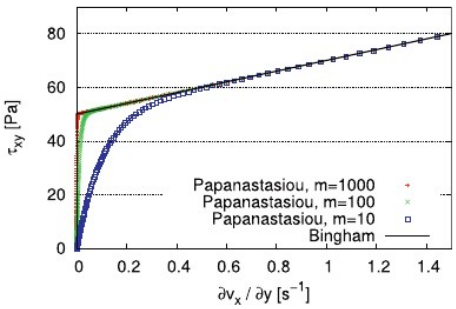

Fig. 1. Papanastasiou approximation of Bingham curve for three different values of regularization parameter m ($\tau_0 = 50Pa$, $\mu = 20Pa \cdot s$).

Linear shape functions are used for approximating both the velocity and the pressure fields. In case of dealing with incompressible materials, this combination does not fulfill the so-called Ladyzenskaja–Babuska–Brezzi (LBB) condition [10] and the problem needs to be stabilized. In this work, the so-called Finite Increment Calculus (FIC) stabilization strategy [49] has been used. The method modifies the continuity equation in a consistent way to stabilize the problem. Details of this method can be found in [49].

The nodal accelerations in Eq. (12) are computed according to the implicit Newmark integration rule [6] as

$$\dot{\bar{\boldsymbol{v}}}^{n+1} = \frac{2}{\Delta t}\left(\bar{\boldsymbol{v}}^{n+1} - \bar{\boldsymbol{v}}^{n}\right) - \dot{\bar{\boldsymbol{v}}}^{n} \tag{14}$$

where Δt is the time increment.

The variation on time of nodal pressures of Eq. (13) is computed as

$$\dot{\bar{\boldsymbol{p}}}^{n+1} = \frac{\bar{\boldsymbol{p}}^{n+1} - \bar{\boldsymbol{p}}^{n}}{\Delta t} \tag{15}$$

The stabilized and fully-discretized form of Eqs. (12) and (13) as well as the implicit solution scheme are reported in Appendix A. At each time step the solution is obtained by a two-step iterative process. More specifically (see also Fig. 2), the increment of the nodal velocities $\Delta\bar{\boldsymbol{v}}$ is first resolved according to Eq. (12). Then, after updating the kinematic variables, the nodal pressures $\bar{\boldsymbol{p}}$ are obtained from Eq. (13). Iterations are performed until the following convergence criterion is fulfilled for both the velocity and the pressure fields

$$e^{a} = \frac{\left\|a_{i+1} - a_{i}\right\|}{\left\|a_{i}\right\|} < 0.0001 \tag{16}$$

where e^{a} is the error associated to variable a, and the subindices refer to the considered non-linear iteration.

3. PFEM Bases

The Particle Finite Element Method (PFEM) is a Lagrangian strategy suitable for large deformation problems. The PFEM was originally proposed to solve Newtonian fluid dynamics problems involving free-surface [29]. In the last decade, the method has been applied to a wide range of engineering problems, such as granular flows [69], melting of polymers [51], fluid-structure interaction (FSI) [71], fluid-soil interaction [48] and landslides [16,61]. The Lagrangian nature of the PFEM enables to capture the computational domain accurately regardless of the extreme deformation. Meanwhile, the efficient remeshing algorithm

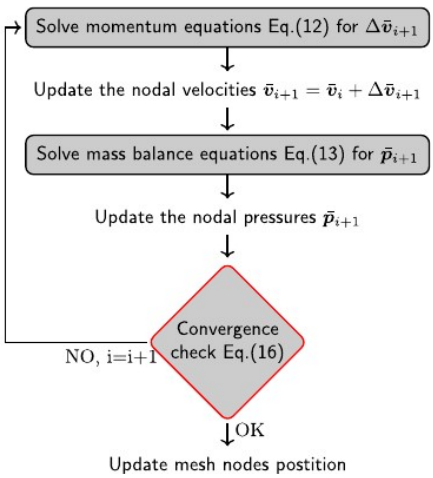

Fig. 2. Schematic representation of the iterative solution of a generic time step. The subindex i represents the iteration number of the implicit solution.

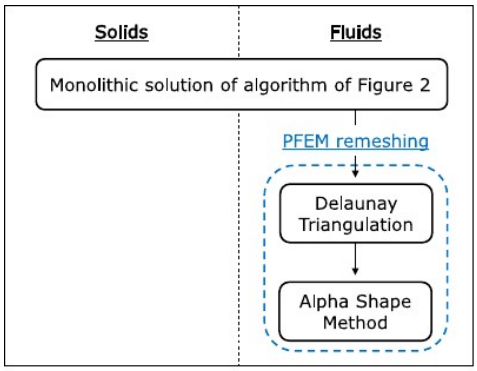

Fig. 3. Solution scheme for a generic step with remeshing.

ensures the preservation of mesh quality for all the duration of the analysis.

Once the nodal positions are updated according to the FEM solution (obtained in this approach as shown in Fig. 2), the quality of the Lagrangian discretization is checked. If the mesh has reached a distortion level higher than an imposed threshold, a new discretization is built. This is done by applying serially the Delaunay Triangulation (DT) [20] and the Alpha Shape (AS) method [19]. The DT rebuilds the discretization ensuring an high quality tessellation. For example in 2D meshes, it maximizes the minimum inner angle and minimizes the maximum one of each triangle. On the other hand, the AS method allows for the recognition of the physical boundaries of the domain. The AS method performs an elemental check for each simplex of the mesh. In particular, the element is erased from the discretization if the following condition is not verified

$$R < \alpha h \tag{17}$$

where R is the circumradius of the element, α is the scalar parameter that gives its name to the method and h is a characteristic length of the mesh. The typical value used for α is around 1.25. Generally, in 3D cases a slightly higher value of the α parameter is chosen. In this work, for the 2D problems α has been set equal to 1.25, while for the 3D ones $\alpha = 1.35$ has been used. See [22] for a dissertation about the role of α and for other details of the PFEM remeshing strategy.

4. PFEM-FEM solution scheme for fluid-solid interaction

The continuous elimination of the finite elements produced by the remeshing, makes the PFEM more suitable for problems in which historical variables do not need to be stored at the element level but on mesh nodes. This explains why a Bingham model can be naturally employed in a PFEM formulation. Note that it is still possible to use the PFEM for constitutive laws depending on historical elemental variables [47,70]. However, in those cases, a procedure for variables mapping from the Gauss points of the previous mesh to the Gauss points of the new one is required, and this may introduce interpolation errors into the numerical scheme. These considerations motivated the use in this work of the standard FEM for the solid solution.

In conclusion, in this approach, fluids and solids are solved monolithically according to the same implicit scheme (see Section 2.2 and Appendix A), but, after updating the nodal positions for both the fluid and the solid, only the fluid domain is remeshed. Fig. 3 represents schematically this solution algorithm.

An admirable feature of the PFEM remeshing rests with its automatic detection of the contact interface between the fluid and the solid domains. During the remeshing procedure, the DT is performed over a cloud of points formed by not only all the fluid nodes, but also those belonging to the rigid walls and to the deformable solids contours, as shown in Fig. 4b. With the following application of the AS method, the new contact elements (elements that are sharing fluid and solid nodes) are identified (Fig. 4c). In this study, the contact elements are computed as fluid elements.

It is important to note that the PFEM remeshing strategy guarantees that, at the interface, fluid and solid nodes are overlapped (see Fig. 4c). This conforming mesh algorithm facilitates the FSI solution, in monolithic as for staggered approaches, because it prevents from the implementation of a mapping strategy to transfer information from one material to the other. For example, in the proposed monolithic approach it is only needed to assemble properly the fluid and solid elemental contributions into the linear system, as for a standard FEM.

Fig. 4 also shows one of the main drawbacks of the PFEM remeshing procedure. In fact, after the creation of the new mesh, new elements may be included in the computational domain, while others may be erased. This induces artificial local changes of the fluid geometry and, globally, a lack of mass conservation. Although this is an endemic problem of the PFEM and it cannot be completely erased, it affects marginally the numerical simulation if a sufficiently fine mesh is used, and there also exist some techniques able to limit its effects [22].

5. Numerical examples

This section shows the application of the proposed numerical approach to several problems involving non-Newtonian fluids. First, the dam break of Bingham fluids against an elastic barrier, is used to analyze several crucial issues of the numerical formulation. Then, two concrete slump tests are simulated in 3D and the numerical results are validated with the experimental ones. Finally, the flow of a bentonite solution over an inclined plane is studied in 2D as in 3D, also considering the impact of a solid object.

5.1. Dam break impact against an elastic barrier

The dam break of a viscous fluid against a deformable membrane is here studied for different values of yield stress in 2D as well as in 3D. The test is used to analyze some important aspects of the proposed numerical approach, such as the mesh and the non-linear convergence, the effect of the regularization parameter m on the numerical results, and the 3D effect given by the lateral confinement. Furthermore, this

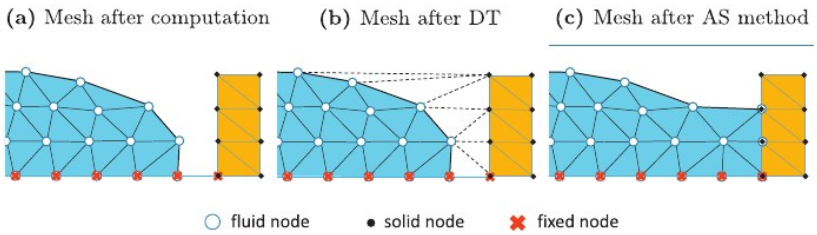

Fig. 4. Representation of the PFEM scheme for detecting the contact with the solid boundaries.

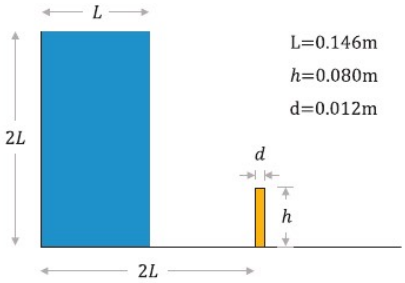

Fig. 5. Dam break against an elastic barrier. Initial geometry.

example aims to show the application of this Lagrangian strategy to an unsteady flow regime and to propose numerical results as benchmarks for 2D and 3D FSI analysis involving Bingham free-surface fluids. The problem is a modification of the benchmark for FSI analysis proposed in [27]. The problem is here analyzed without the vertical wall located behind the elastic membrane and for a reduced duration of 0.5 s. During this time period, the motion of the barrier is not affected by the wave created by that vertical wall, so the results are comparable to the ones of the benchmark [27]. These modifications have been done in order to reduce the uncertainty of the numerical results. In fact, as shown in a recent analysis of the benchmark problem [41], after 0.5 s the numerical results start to diverge as a consequence of the fluid unsteadiness and the different prediction of the first impact. This makes almost meaningless to use the second part of the example for validation purposes. The authors believe that the capability to reproduce accurately the first impact of the fluid stream against the barrier is crucial to determine the efficiency of the method.

The initial 2D geometry of the problem is given in Fig. 5.

Both 2D and 3D non-Newtonian problems have been studied for three values of yield stress, namely 25 Pa, 50 Pa and 100 Pa. Also the Newtonian case, corresponding to $\tau_0 = 0$ Pa, has been analyzed for comparison purposes. The rest of material properties are the same as in [27]. The fluid and solid data are collected in Table 1. No-slip conditions have been considered for the rigid walls.

5.1.1. Mesh convergence

The convergence analysis is performed for the 2D problem using $\tau_0 = 100$ Pa. Six different mean mesh sizes h have been considered. Each discretization has a different number of elements in the solid width. The finest one ($h = 0.002$ m) has 24,376 fluid elements and 6 elements along the membrane width. The coarsest one ($h = 0.012$ m) is composed of 642 fluid elements and only one element in the solid width. The coarsest and the finest meshes are shown in Fig. 6.

Table 1
Dam break against an elastic barrier. Fluid and solid data.

Fluid data			Solid data		
ρ [kg/m^3]	μ [$Pa \cdot s$]	τ_0 [Pa]	ρ [kg/m^3]	E [MPa]	ν [-]
1000	0.001	0, 25, 50, 100	2500	1	0

Fig. 7a shows the evolution of the horizontal maximum displacement of the cantilever obtained with the six tested discretizations. On the other hand, the results plotted in Fig. 7b focus on the fluid dynamic problem only and represent the evolution on time of the fluid front position for the period preceding the impact against the deformable obstacle.

In Fig. 8a the maximum horizontal deflection of the membrane is given as a function of the number of elements, while Fig. 8b plots the percentage error, computed with respect to the solution obtained with the finest mesh, as a function of the mesh size.

The graphs show clearly the convergence behavior of the numerical formulation. Furthermore, they show that while the fluid dynamic problem could be solved with a relatively coarse mesh (the discretization with $h = 0.004$ m approximates well the solution obtained with the finest mesh), a much finer mesh is required to simulate accurately the FSI. As shown in Fig. 8b, the deflection computed with $h = 0.004$ m is almost the 10% smaller than the one obtained with $h = 0.002$ m. Note that, in the present conforming mesh approach, this affects the choice of the fluid mesh size. In fact, in order to avoid topological inconveniences, such as the overlapping of fluid and solid meshes or the penetration of fluid particles into the solid domain, the fluid mesh close to the fluid-solid interface must have a size similar to the solid one.

5.1.2. Non-linear convergence

It is well known that non-Newtonian models increase the non-linearity of the Navier–Stokes problem. In this sense, it is important to analyze the non-linear convergence of the proposed implicit strategy. In order to have an overview of the convergence behavior of the numerical method, the non-linear convergence is analyzed at four time instants (t = 0.05 s, 0.15 s, 0.3 s, 0.5 s), corresponding to different phases of the dam break problem. The convergence analysis is performed for the same problem analyzed before ($\tau = 100$ Pa and $h = 0.002$ m).

Fig. 9 collects the velocity and pressure errors computed using Eq. (16). The graphs show that the convergence of the pressure field is generally slower than the one of the velocity field. The worst convergence is exhibited at $t = 0.3$ s (5 iterations for the velocity and 10 for the pressure). This is due to the high non-linearity of the problem at this stage. In particular, the fluid shows huge splashes and the solid obstacle has just reached the maximum deflection. In all other cases, the iterations are no higher than 6. This convergence behavior is reasonable, considering the high non-linearity introduced by both the Papanastasiou model and the FSI, and it is close to the one shown by the same

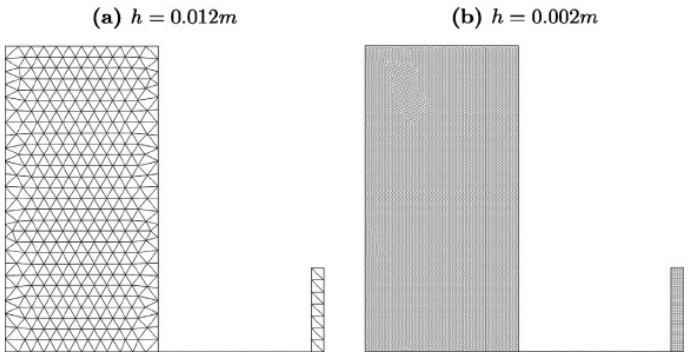

Fig. 6. Dam break impact against an elastic barrier ($\tau_0 = 100$ Pa). Coarsest and finest meshes used for the convergence study.

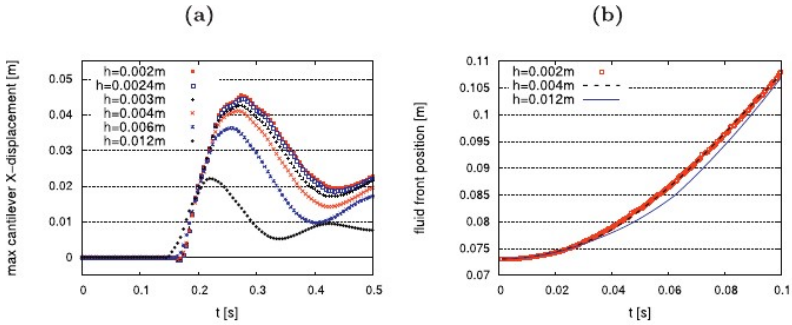

Fig. 7. Dam break impact against an elastic barrier ($\tau_0 = 100$ Pa). Evolution on time of the cantilever horizontal displacement (*a*), and fluid front (*b*).

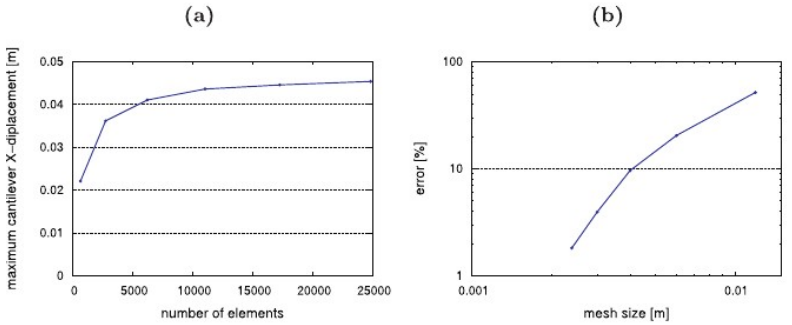

Fig. 8. Dam break impact against an elastic barrier ($\tau_0 = 100$ Pa). (*a*) Maximum solid deflection obtained with the six different meshes. (*b*) Percentage error computed with respect to the finest mesh solution.

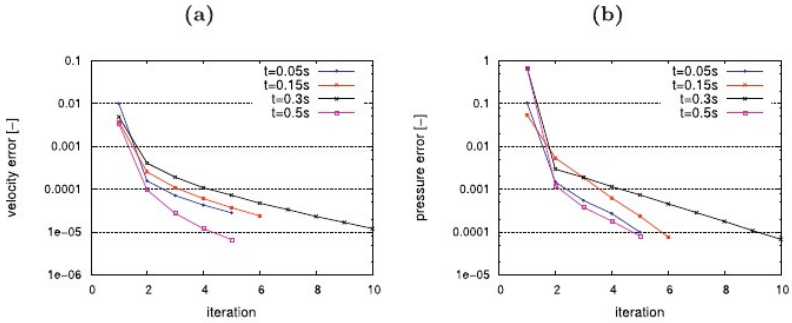

Fig. 9. Dam break impact against an elastic barrier ($\tau_0 = 100$ Pa). Errors of velocity (*a*) and pressure (*b*) fields at the non-linear iterations at four time instants.

FIC-stabilized PFEM method to reach the convergence in Newtonian fluids problems [49], where generally the convergence was reached after 5 iterations. This confirms the efficiency and generality of the proposed stabilized method.

Note that the non-linear convergence has also effects on the mass preservation properties of the numerical strategy. In this specific case, the overall mass variation after 0.5 *s* is 1.196% of the initial mass. In particular, the non-linear computation produces an increment of mass equal to 1.734%, whereas the remeshing procedure induces a loss of 0.538%. This can be considered a small value for such an unsteady and non-linear problem. Furthermore, this magnitude of mass variation is analogous to the one shown in [49] for Newtonian fluids analysis. This is a further confirmation of the validity of the FIC-stabilized Lagrangian formulation for treating also non-Newtonian fluids.

5.1.3. Effect of regularization parameter m

As already explained in Section 2.1 and illustrated in Fig. 1, the Papanastasiou's regularization parameter *m* affects the accuracy of the ap-

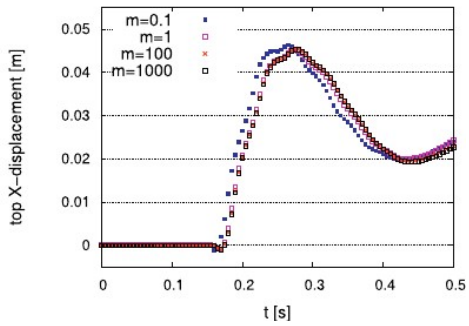

Fig. 10. Dam break impact against an elastic barrier ($\tau_0 = 100$ Pa). Evolution on time of the horizontal deflection of the elastic barrier obtained for four different values of the Papanastasiou's regularization parameter *m*.

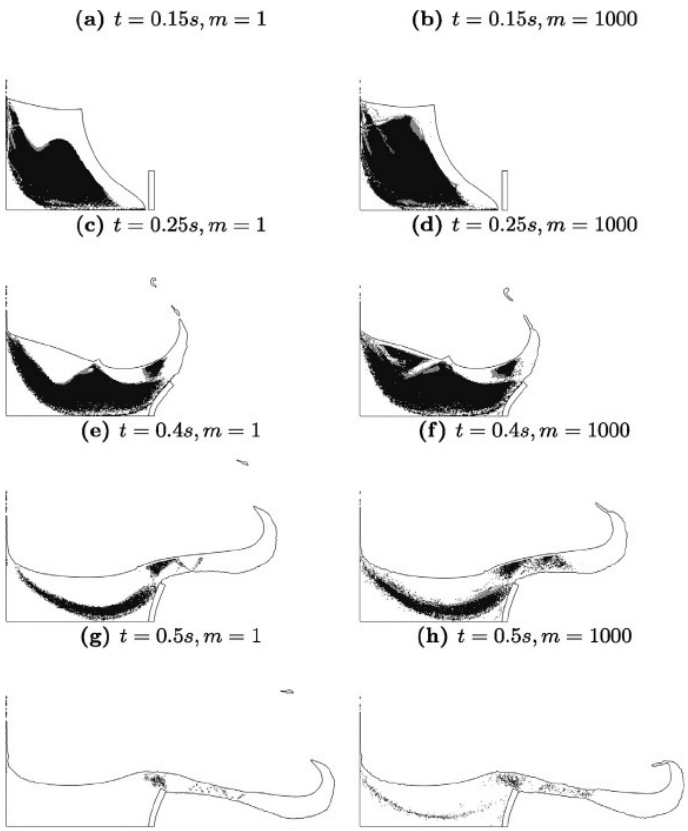

Fig. 11. Dam break impact against an elastic barrier ($\tau_0 = 100$ Pa). Yielded elements are plotted with black color. Results for $m = 1$ and $m = 1000$.

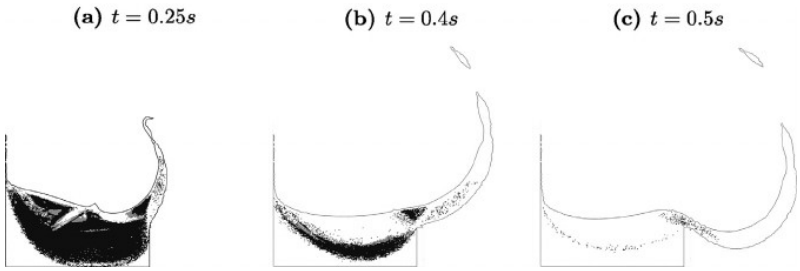

Fig. 12. Dam break impact against a rigid barrier ($\tau_0 = 100\ Pa,\ m = 1000$).

proximation of the Bingham curve. In particular, higher values of m are needed to approximate well the rigid behavior. However, the parameter m also affects the quality of the algebraic system. In fact, if a big regularization parameter is used, large values of viscosity are introduced into the linear system and this may deteriorate its conditioning. Hence, m cannot be chosen as large as desired. With the aim of analyzing the effect of the regularization parameter on the numerical results, the dam break problem is solved with four different values of m, spanning from 0.1 to 1000. Fig. 10 collects the results obtained with the four tested values of m.

The graph shows that the solutions obtained with $m = 100$ and $m = 1000$ are almost identical, while some discrepancies are exhibited for $m = 0.1$. However, it is worth to note that the effect of m depends highly on the numerical test taken in consideration. In this specific test, the fluid is suffering from large strain rates during the whole analysis and this explains the reduced effect of the regularization parameter. Indeed, the role of m is crucial for fluids close to the state of rest or, more generally, when the shear rate is small, as in the example that will be analyzed in Section 5.3.

The regularization parameter m also affects the demarcation between the yielded and un-yielded zones. For smaller values of m, an higher strain rate is required to reach the yield value τ_0. This is confirmed by the results plotted in Fig. 11 that show the yielded elements (drawn in black) obtained for $m = 1$ and $m = 1000$ at four time instants.

As expected, the yielded regions obtained with $m = 1$ are smaller than the ones obtained with $m = 1000$. Despite that, globally, the differences between the two analyses are reduced.

To show the potential of the proposed formulation to design protection barriers, the problem is also solved considering the obstacle as rigid. In Fig. 12 three snapshots of the simulation are given.

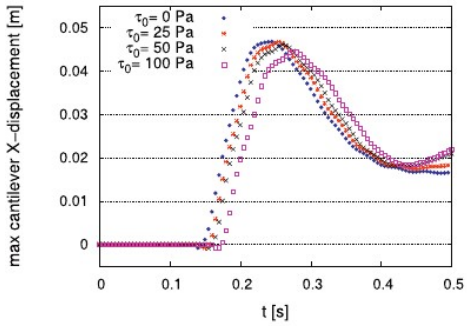

Fig. 13. Dam break impact against a elastic barrier (mesh size $h = 0.002\ m$). Evolution on time of the maximum horizontal displacement of the barrier for four values of τ_0.

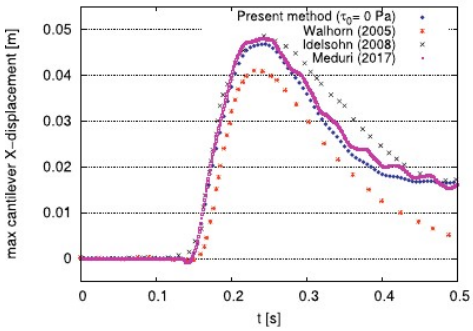

Fig. 14. Dam break against an elastic barrier ($\tau_0 = 0$ Pa, $h = 0.002$ m). Evolution on time of the maximum horizontal displacement of the barrier. Comparison to Walhorn et al. [27], Idelsohn et al. [28] and Meduri et al. [41].

By comparing Fig. 12 and the left column of Fig. 11, it arises that with the rigid barrier the stream arises an higher altitude and a reduced horizontal runout than the case with flexible membrane. Concerning the yielded elements, a similar pattern is obtained.

5.1.4. Effect of τ_0

The finest mesh has been used for testing the effect of the yield stress τ_0 on the numerical results. In Fig. 13 the horizontal deflection of the elastic cantilever obtained for four values of τ_0 is plotted. The results show that higher values of τ_0 delay the collision of the fluid stream against the elastic object and reduce its inertial force. As a consequence, the maximum horizontal displacement of the cantilever also reduces for increasing values of τ_0.

The case of $\tau_0 = 0$ Pa corresponds to the Newtonian problem already analyzed in [23]. In Fig. 14, the time evolution of the horizontal displacement of the top of the elastic membrane obtained with $h = 0.002\ m$ is compared to the results presented in [27,28,41].

The 2D results show a good agreement to those in the literature, confirming the efficiency of the Unified formulation for solving FSI problems.

5.1.5. 3D lateral effects

In order to analyze the effect of lateral containment on the dam break evolution, the problem is solved in 3D considering the channel width equal to the height of the obstacle (0.8 m). No-slip conditions are considered for all the rigid walls. The same mean mesh size $h = 0.003$ m (4 elements along the elastic membrane width) has been used for the 2D and the 3D simulations, leading to 11,050 triangular finite elements

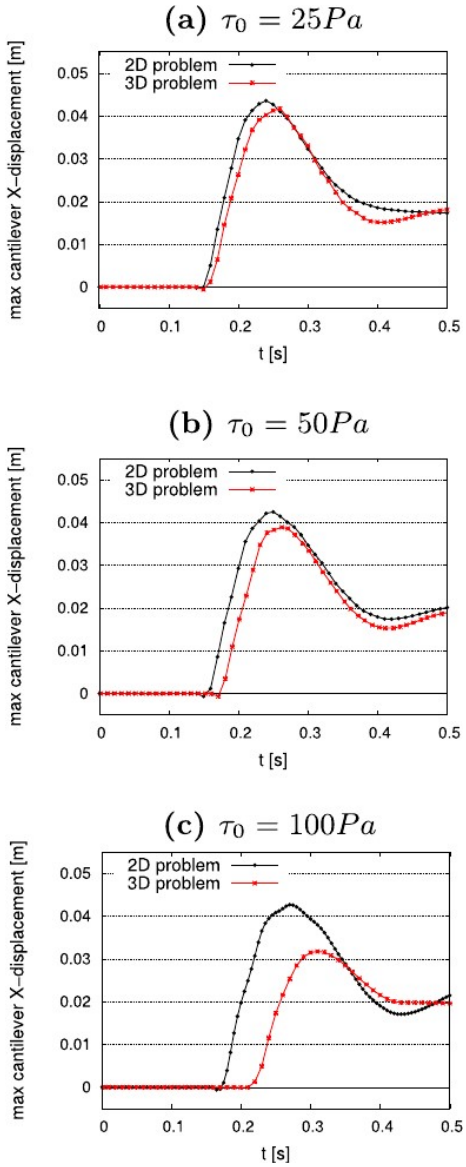

Fig. 15. Dam break against an elastic barrier (mesh size $h = 0.003$ m). Evolution on time of the horizontal displacement at the top of the barrier for three different values of yield stress. 2D and 3D results.

for the 2D problem and 801,597 tetrahedra for the 3D case. Fig. 15 collects the results of the 2D and 3D non-Newtonian problems obtained for three different values of the yield stress, namely $\tau_0 = 25, 50, 100$ Pa.

The results show that, differently from the 3D example that will be presented in Section 5.3, the plane strain hypothesis is not valid for this non-Newtonian problem. The lateral containment reduces the velocity of the fluid flow and, consequently, its impact force against the solid membrane is reduced. As shown in the graphs of Fig. 15, the discrepancy between the 2D and 3D results grows by increasing the yield stress.

In Fig. 16, the 3D results for $\tau_0 = 100$ Pa are given for three time instants. The velocity contours are plotted over the fluid and solid computational domains.

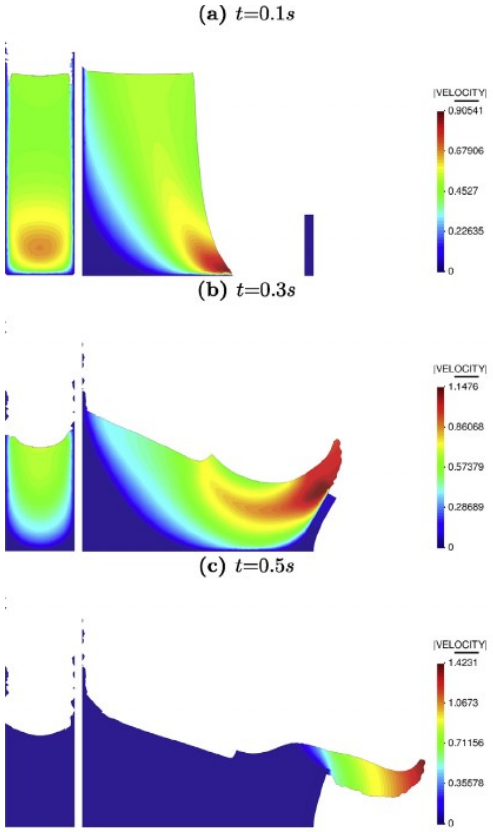

Fig. 16. Dam break against an elastic barrier (τ_0 = 100 Pa). 3D results at three time instants. Pictures in left-hand column show the section yz located at x = 0.148 m. Pictures in right-hand column refer to the section xy located at x = 0.04 m.

The transversal cut at x=0.148 m, represented in the left pictures of Fig. 16, shows clearly the resistance exerted by the lateral containment on the fluid motion. Consequently, the deflection of the 3D elastic membrane is reduced and the horizontal distance reached by the fluid stream is also limited.

5.2. Fresh contrete slump tests

The slump test is a standard laboratory experiment used to determine the so-called workability of fresh concrete. The test consists of filling a conical container with concrete and measuring the evolution of its shape after the removal of the rigid container. The test ends when the fresh concrete reaches a static state. In these tests, the values of interest are the slump and the spread of the concrete. The former is the difference between the initial and the final fluid height, whereas the latter is the difference between the initial and the final diameter measured at the base of the cone [58]. Two standard and widely used slump tests, such as the so-called Abrams [11] and mini cone [12] tests, are analyzed in this section. The initial geometry of the slump is illustrated in Fig. 17.

Instead of an homogeneous material, the fresh concrete is composed by a suspension of solid grains in a fluid matrix. From the computational point of view, this opens two possibilities, namely, either computing it as a one-phase fluid material, or modeling it considering the interaction with the particles suspended in the fluid. An overview regarding the different computational techniques for fresh concrete modeling has been made in [59]. In this work, the former approach is used. Furthermore,

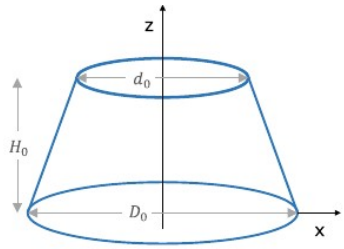

Fig. 17. Initial cone shape for slump tests.

Table 2
Abram slump test. Geometrical and material data.

Geometrical data			Material data		
H_0 $[m]$	D_0 $[m]$	d_0 $[m]$	ρ $[kg/m^3]$	μ $[Pa{\cdot}s]$	τ_0 $[Pa]$
0.3	0.2	0.1	2200	255	32

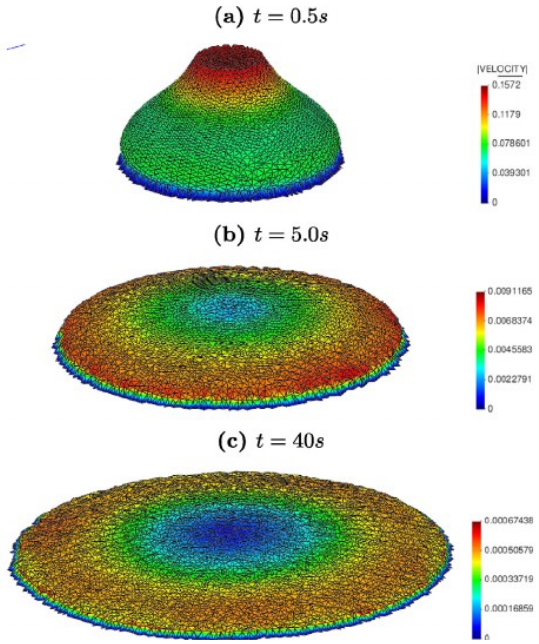

Fig. 18. Abram slump test. Velocity contours plotted over the deformed configuration at three different time instants.

both slump tests are modeled considering null the interaction with the container and no-slip conditions for the rigid plan over which the fresh concrete spreads. The regularization parameter m of the Papanastasiou model is set equal to 1000 in both cases.

5.2.1. Abram test

The Abram slump test is generally used for fresh concrete rather than cement pastes [58]. The geometry information and the material parameters are provided in Table 2.

The problem has been solved in 3D using tetrahedral meshes of three different sizes in order to verify the convergent behavior of the method and to assess the reliability of the PFEM results of the finest mesh. Specifically, the mean mesh sizes used in the simulations are 0.015 m, 0.01 m and 0.0075 m, corresponding to 15900, 54464, and 129818 tetrahedra, respectively.

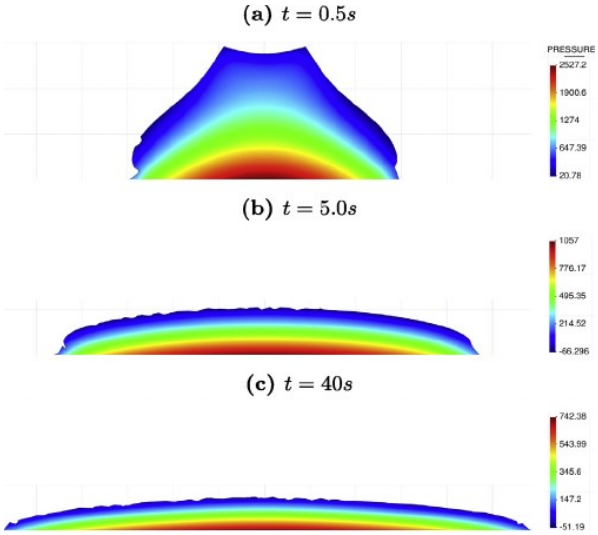

Fig. 19. Abram slump test. Pressure contours plotted over the central section at three different time instants.

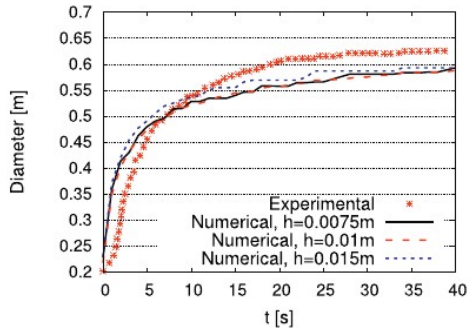

Fig. 20. Abram slump test. Evolution on time of the spreading diameter obtained for three different meshes. Experimental values from [14].

In Fig. 18 three representative snapshots of the simulation are provided. The velocity contours are plotted over the deformed configuration of the fluid at the time instants $t = 0.5$ s, $t = 5.0$ s and $t = 40$ s.

As shown, the material flows immediately when the container is removed, and the whole process proceeds in an axisymmetric manner as expected. The top surface first owns the maximum velocity shortly after the release (Fig. 18a), which however decreases as the spreading proceeds (Fig. 18b). Fig. 18c shows the deposit of the fresh concrete at the last instant of the numerical simulation (t=40 s). At this stage, the material diameter is almost three times larger than the initial one and the material flow is very close to stop (the material velocity is smaller by three orders of magnitude than the velocity obtained at the initial phase of the test).

Fig. 19 shows the pressure contours of the section XZ for the same time instants considered in Fig. 18. The pictures show that the middle part of the flow always possesses the maximum pressure throughout the whole slumping procedure.

The graph of Fig. 20 shows the evolution on time of the spreading diameter obtained numerically with three different meshes and experimentally using the 4C-Rhometer [67], as reported in [14]. Although there exists a certain discrepancy with respect to the experimental results, the 3D numerical simulation shows an acceptable agreement, even when relatively coarse meshes are in use. This validates not only the use of a single-phase approach for modeling this multi-phase material, but also the three-dimensional PFEM framework developed in this study.

Table 3
Mini cone slump test. Geometrical and material data.

Geometrical data			Material data		
H_0 [m]	D_0 [m]	d_0 [m]	ρ [kg/m^3]	μ [$Pa \cdot s$]	τ_0 [Pa]
0.05	0.1	0.07	2252	4.018	18.0182

It is worth commenting about the small jumps shown in the numerical curves of Fig. 20. These are due to the PFEM way of modeling the fluid advancement. With the PFEM, the fluid front motion is determined by the creation of a new boundary element and not by the slip of the wall nodes (as shown in Fig. 4) and this produces the non-smoothness of the front evolution curve. See [22] for a detailed analysis of this and other issues related to the PFEM remeshing, such as the non-smoothness of the free-surface or the fluid adherence/departure from/to the solid boundaries.

5.2.2. Mini cone test

The mini cone slump test [12] is generally used to determine the workability of cement pastes. Table 3 shows the information regarding the geometry and the material properties.

A total of 105187 tetrahedra has been used for the PFEM solution. Fig. 21 shows four time instants of the 3D simulation. To show more clearly the stoppage of the fluid, a threshold of 0.0005 m/s is imposed to the velocity norm contours plotted in the figures. If the nodal velocity norm exceeds that limit, the red color is plotted. As illustrated, the slumping procedure is similar to that observed in the Abram test, however, due to the reduced viscosity of the cement paste, the slump is accelerated. In Fig. 22, the time evolution of the fluid diameter of the material is plotted and compared to the expected final diameter according to the experimental test [67] (D = 0.2249 m) and to that obtained considering the axisymmetric approximation in [14] (D=0.220 m). The graph shows that the proposed computational method is capable to predict the total spread of the cement past with a very good accuracy. The graph also shows that, even if a Papanastasiou formulation cannot reproduce exactly the quiescent state, one can easily understand when the stoppage of the fluid flow occurs, at least for the used value of the regularization parameter ($m = 1000$). In this specific case, it can be assumed that the fluid reaches a state of rest after around 5 s the releasing of the container.

5.3. Flow of a bentonite solution on a slope

In [13] a series of experimental results for the flow of a bentonite solution over an inclined plan is reported. In this work, two of these laboratory tests have been reproduced and called *Case A* and *Case B*. The schematic illustration of the test is shown in Fig. 23.

In [13] the bentonite solution has been characterized by two values of apparent yield stress, the biggest one, τ_l, for the loading process and the smallest one, τ_u, for the unloading process. In this time-independent model, the two cases have been analyzed separately. The experimental results are thus expected to lay between the two limit analyses. Also the case with a mean value of yield stress ($\tau_m = 0.5\tau + 0.5\tau_l$) has been studied. The regularization parameter $m = 1000$ has been used in all the analyses. In Table 4 the initial geometrical data and the material parameters are given for both tests.

Case A and *Case B* have been studied for the three different values of yield stress (τ_u, τ_l and τ_m) and assuming plane strain conditions. In addition, with the aim of verifying the validness of the plane strain assumption, the most viscous problem, *Case A*, has been studied also considering the actual 3D geometry of the experimental test (width of 0.34 m) for τ_m. In all the cases, no-slip conditions have been considered for the rigid walls.

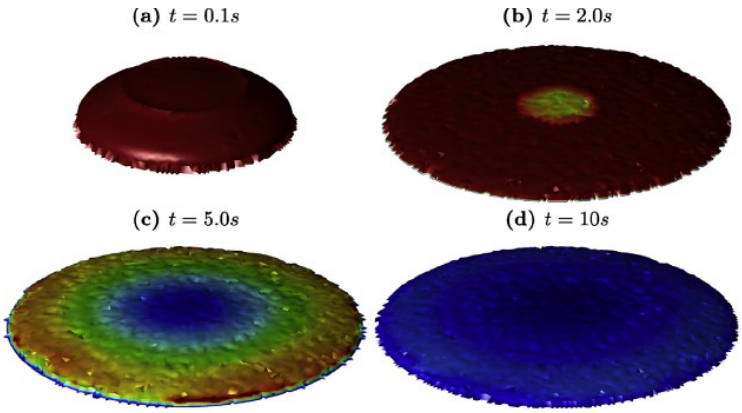

Fig. 21. Mini cone slump test. 3D results for four time instants. The nodal velocity norm contours are plotted over the deformed configurations. For values higher than 0.0005 *m/s*, the red color is plotted. (For interpretation of the references to colour in this figure legend, the reader is referred to the web version of this article.)

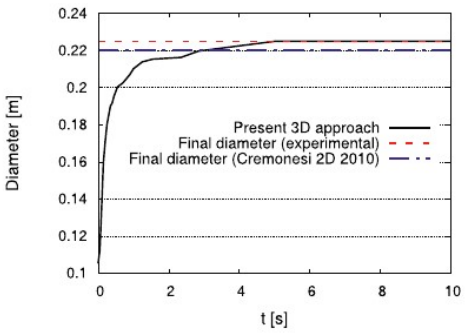

Fig. 22. Mini cone slump test. Time evolution of material diameter. Comparison to the expected final diameter according to the experimental test [67].

As in [13], the flow evolution has been studied according to two dimensionless variables, the dimensionless front position x^* and the dimensionless time t^*. These variables are computed, respectively, as

$$x^* = X / H_0 \tag{18}$$

where X is the front wave location, which is null at the initial time instant, and

$$t^* = t\sqrt{g/H_0} \tag{19}$$

where g=9.81 m/s^2 is the gravity acceleration.

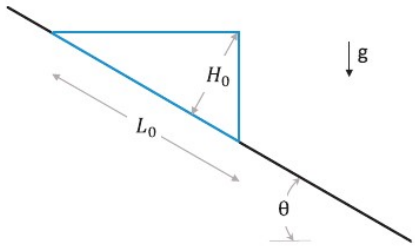

Fig. 23. Flow of a bentonite solution over a slope. Initial geometry.

Table 4
Flow of a bentonite solution over a slope. Geometrical and material data.

	Geometrical data			Material data		
	L_0 [m]	H_0 [m]	θ [^{0}]	ρ [kg/m^3]	μ [$Pa{\cdot}s$]	$\tau_0 - \tau_l$ [Pa]
Case A	0.3024	0.0756	15	1085.1	0.635	21.1 - 165
Case B	0.2928	0.0732	15	1085.1	0.555	14 - 50

The dimensionless time evolution of the dimensionless front position x^* of *Case A* and *Case B* is plotted in Fig. 24a and Fig. 24b, respectively.

The graphs show that, with the exception of the initial phase of the flow of *Case B*, the experimental results are globally bounded by the two limit cases given by $\tau_0 = \tau_l$ and $\tau_0 = \tau$. Furthermore, a very good accordance between the 3D and 2D results of *Case A* is obtained for

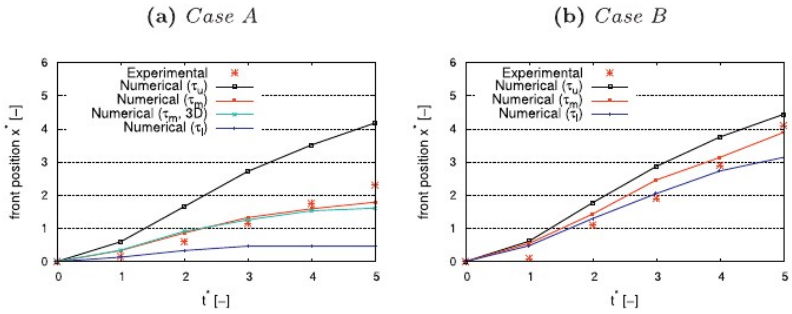

Fig. 24. Flow of a bentonite solution over a slope. Evolution on dimensionless time t^* of the dimensionless front position x^*. Numerical results for $\tau_0 = \tau$, τ_l, τ_m and experimental results.

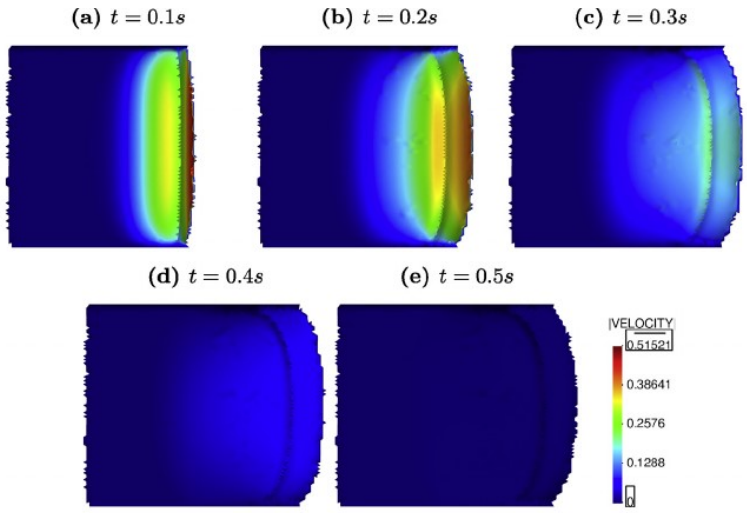

Fig. 25. Flow of a bentonite solution over a slope. *Case A*, 3D simulation with $\tau_0 = \tau_m$. Velocity contours plotted over the fluid flow.

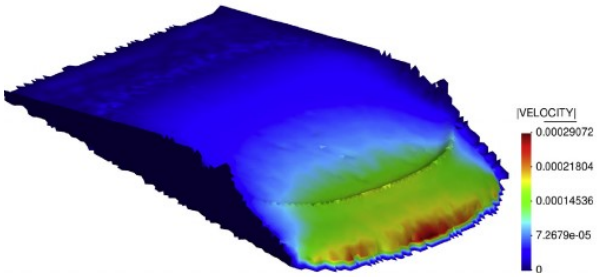

Fig. 26. Flow of a bentonite solution over a slope. Final configuration for the 3D simulation of *Case A* with $\tau_0 = \tau_m$.

$\tau_0 = \tau_m$. This shows that the lateral boundaries are sufficiently far to not affect the fluid motion at the central zone of the flow, and the problem can be studied with a 2D model reducing highly the computational cost.

The numerical results of the 3D analyses of *Case A* are plotted for five time instants in Fig. 25, from the vertical view, while Fig. 26 shows the 3D view of the fluid at $t = 0.5s$.

The effect of regularization parameter m is analyzed for the *Case A* and $\tau_0 = \tau_m$. Three different values of m have been analyzed, namely 1, 100, 1000. In Fig. 27 the free-surface position obtained for the three analyses at four time instants is plotted. The pictures show that the solution obtained with $m = 100$ and $m = 1000$ are almost identical. On the other hand, for $m = 1$ the fluid spread is sensibly larger than the other two cases. After 1 s of analysis the fluid is still flowing, whereas it is practically stopped for $m = 100$ and $m = 1000$. This analysis shows clearly that, in problems dominated by low shear rates, the regularization parameter of the Papanastasiou model is of paramount importance to reproduce accurately the rigid behavior of the Bingham model. In these cases, a large value of m (*e.g.* $m \geq 100$) is recommendable.

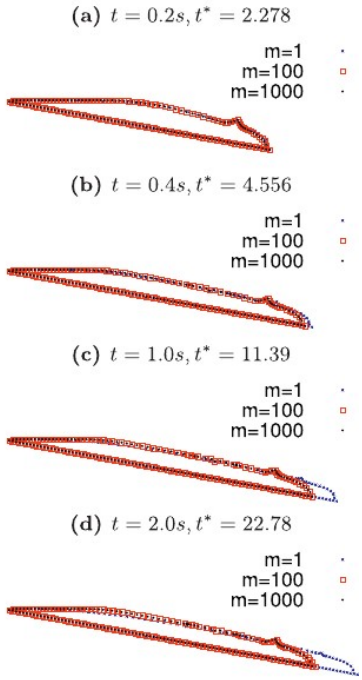

Fig. 27. Flow of a bentonite solution over a slope. Fluid contours at four time instants obtained for $m = 1, 100, 1000$.

5.4. Impact of a falling object over a bentonite solution flow

The 3D problem studied in the previous example (*Case A* with $\tau_0 = \tau_m$) is here analyzed considering the impact of a solid block of density $\rho = 200$ Kg/m^3, modeled as an hypoleastic material (Young modulus $E = 10^7$ MPa and Poisson ratio $\nu = 0$). The physical phenomena reproduced by this numerical simulation may be representative of those of natural hazards triggered by dynamic impacts. The purpose of this example is to show that the proposed computational framework is capable of dealing with complex 3D dynamic fluid-solid interactions. The solid block has a parallelepiped shape, with the base $d = 0.1$ m, height $h = 0.05$ m and width $w = 0.15$ m, and is falling from an height $z = 0.2$ m, as represented in Fig. 28.

The initial mesh used for the computation is composed by 172729 and 12947 fluid and solid elements, respectively. Three time instants of the 3D simulation are illustrated in Fig. 29 by showing only the central vertical cut of the fluid and solid domains. The impact between the solid block and the fluid flow occurs at around $t^* = 2$ (corresponding to $t =$

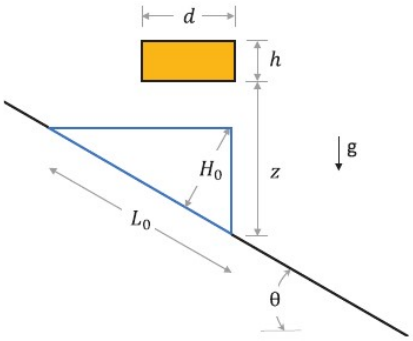

Fig. 28. Impact of a falling object over a bentonite solution flow. Initial geometry.

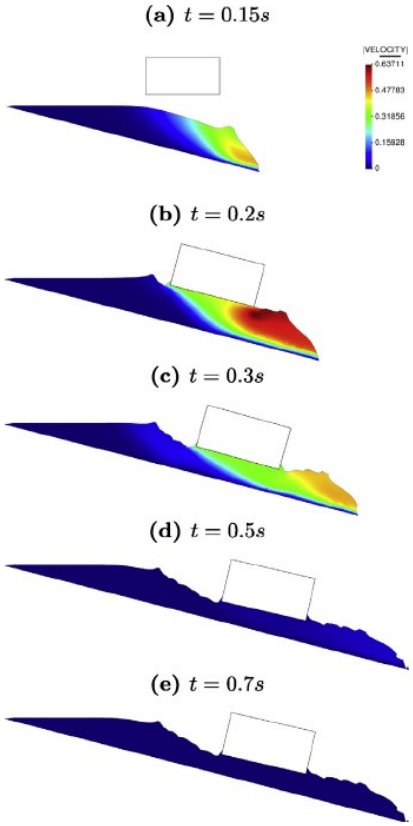

Fig. 29. Impact of a falling object over a bentonite solution flow. Central cut of fluid and solid. Velocity norm contours plotted over the fluid configuration.

0.175 s). Fig. 29a shows that the impact induces a clear shear band in the fluid flow and a sudden acceleration at its frontal part. This is also confirmed by the graph of Fig. 30, which compares the evolution on time of the front position obtained with the fluid analysis presented in the previous section, and this FSI problem.

Fig. 31 gives two different views of the final configuration of the FSI problem to show more clearly the effect of the solid impact on the flow.

6. Conclusions

This work aims to present a Lagrangian method for the 3D modeling of Fluid-Structure Interaction (FSI) problems with free-surface Bingham

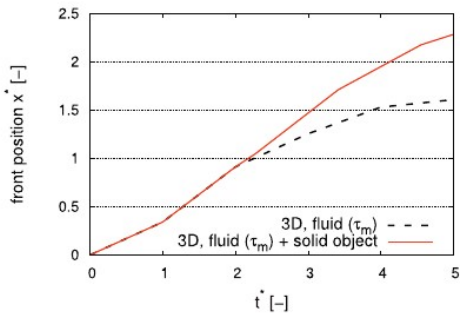

Fig. 30. Impact of a falling object over a bentonite solution flow. Dimensionless time t^* evolution of the dimensionless front position x^*.

fluids. The formulation uses the Particle Finite Element Method (PFEM) to deal with materials that suffer from large deformations and to detect the contact interface between the fluid and the elastic structures. The fluid parts of the domain are computed according to a Papanastasiou model that has been implemented into a stabilized Velocity-Pressure strategy [49], whereas for solids an hypoelastic model is used. The FSI problem is solved monolithically in the Unified formulation spirit [23].

The accuracy, versatility and robustness of the method have been shown by simulating several 2D and 3D problems involving different types of fluid flow regimes and fluid-solid interactions.

First, a series of Bingham fluid dam break against a deformable membrane has been studied, considering both a 2D and a 3D geometry. The numerical test has been used to analyze several crucial issues of the numerical formulation. First, the convergent behavior with mesh refinement has been shown for both the fluid dynamics and the FSI problem. Then, the non-linear convergence of the method has been studied for the finest tested mesh. It has been shown that the pressure field exhibits a slower convergence than the velocity one. In the worst case, the pressure convergence is reached after 10 iterations, while, for the rest of the cases, 6 iterations are enough to converge. These results are reasonable considering the high non-linearity of this FSI problem and prove the effectiveness of the proposed stabilized method for non-Newtonian fluid analysis. The effect of the regularization parameter m has also been analyzed. In this specific case, the effect of m is limited, although a certain discrepancy is shown with respect to the yielded surface identification obtained for different values of m. The robustness of the formulation has been tested considering different values of the yield stress τ_0. As expected, increasing τ_0, the fluid impacts later the elastic barrier and with a lower impact force. For null yield stress, the numerical results of the Unified formulation have been shown to be in accordance with those available in the literature [23]. Finally the effect of lateral containment has been studied by solving the same problem in 2D and in 3D for different values of yield stress. It has been shown that the plane strain hypothesis cannot be used to approximate the solution obtained with the considered 3D geometry. Furthermore, it has been shown that the discrepancy between the 2D and 3D results grows by increasing τ_0.

Then, two standard fresh concrete slump tests, such as the Abram and mini cone, have been studied considering their real 3D geometries. A good agreement between the numerical and experimental results has been obtained for both tests. The Abram slump test has been also analyzed using different tetrahedral meshes, and the convergence behavior of the numerical results has been verified.

In the following analysis, the flow of a bentonite solution over an inclined plane has been studied for two different fluid compositions and initial geometries. The two tests have been taken from [13], where the minimum and maximum values of yield stress are given for each experimental test. Both limit situations have been studied. It has been shown

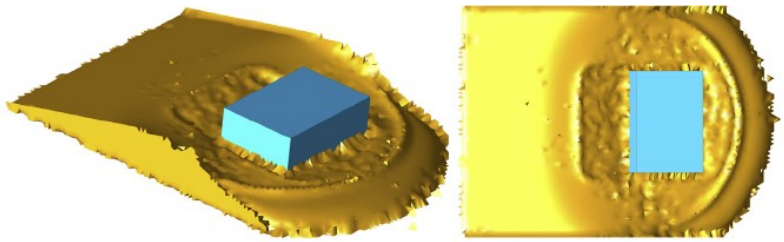

Fig. 31. Impact of a falling object over a bentonite solution flow. Two views of the final configuration.

that the experimental results are bounded by the numerical results obtained with the two limit values of yield stress, with the exception of the first instants of the less viscous case. Moreover, the validity of plane strain hypothesis has been assessed by solving the most viscous problem with the 3D geometry and by showing the accordance between the 2D and 3D solutions. As for the first example, the effect of the regularization parameter has been studied. In this case. that is characterized by lower shear rates than the previous one, the parameter m affects more the numerical results. For low values of the regularization parameter (*e.g.* $m<100$), the model cannot reproduce accurately the fluid stoppage. On the other hand, for $m\geq 100$, it has been shown that the state of rest can be easily recognized from the numerical results.

The same bentonite solution flow has been then studied under the impact of a falling solid object. This situation can be considered representative of landslides or avalanches triggered by the dynamic impacts of solid objects. The proposed numerical method has demonstrated to be capable of dealing with such a complex interaction by reproducing the shear band and sudden acceleration of the fluid flow induced by the impact of the object.

Acknowledgment

The first author, beneficiary of an AXA Research Fund post-doctoral grant, acknowledges the company for its economic support. The second author also wishes to acknowledge the support of European Commission H2020 Marie Sklodowska-Curie actions individual fellowship (Reference 744281).

Appendix A. Fully linearized form and solution scheme

At each computational step, the linear momentum (Eq. (1)) and the continuity (Eq. (2)) equations are solved iteratively for the nodal increments of velocity and the pressures, respectively. The following enumeration describes the solution strategy for a generic time step $[{}^n t; {}^{n+1}t]$ of duration Δt (subscripts 's' and 'f' refer to solid and fluid elements, respectively)

1. At each non-linear iteration i:
2. Compute the nodal velocity increments $\Delta\bar{\boldsymbol{v}}$:
   (a) $\boldsymbol{K}^i\Delta\bar{\boldsymbol{v}} = \boldsymbol{R}^i(\bar{\boldsymbol{v}}^i, \bar{\boldsymbol{p}}^i)$
   (b) where $\boldsymbol{K}^i = \boldsymbol{K}^m(\bar{\boldsymbol{x}}^i, \boldsymbol{c}_{f,s}) + \boldsymbol{K}^\rho(\bar{\boldsymbol{x}}^i)$
3. Update nodal velocities: ${}^{n+1}\bar{\boldsymbol{v}}^{i+1} = {}^{n+1}\bar{\boldsymbol{v}}^i + \Delta\bar{\boldsymbol{v}}$
4. Update nodal coordinates: ${}^{n+1}\bar{\boldsymbol{x}}^{i+1} = {}^{n+1}\bar{\boldsymbol{x}}^i + \bar{\boldsymbol{u}}(\Delta\bar{\boldsymbol{v}})$
5. Compute the nodal pressures $\bar{\boldsymbol{p}}^{i+1}$: $\boldsymbol{H}\,\bar{\boldsymbol{p}}^{i+1} = \boldsymbol{F}_p(\bar{\boldsymbol{v}}^{i+1}, \bar{\boldsymbol{p}}^i)$
   (a) where $\boldsymbol{H} = \left(\frac{1}{\Delta t}\mathbf{M}_1 + \frac{1}{\Delta t^2}\mathbf{M}_2 + \mathbf{L} + \mathbf{M}_b\right)$
   (b) and $\boldsymbol{F}_p = \frac{\mathbf{M}_1}{\Delta t}{}^n\bar{\boldsymbol{p}} + \frac{\mathbf{M}_{2f}}{\Delta t^2}\left({}^n\bar{\boldsymbol{p}} + {}^n\dot{\bar{\boldsymbol{p}}}\Delta t\right) + \mathbf{Q}^T\,\bar{\boldsymbol{v}}^{i+1} + \boldsymbol{f}_p$
6. Compute the Cauchy stresses: $\boldsymbol{\sigma}^{i+1}$
7. Check the **convergence**: $\frac{\|\Delta\bar{\boldsymbol{v}}^{i+1}\|}{\|{}^n\bar{\boldsymbol{v}}\|} \leq 0.0001$, $\frac{\|\bar{\boldsymbol{p}}^{i+1} - \bar{\boldsymbol{p}}^i\|}{\|{}^n\bar{\boldsymbol{p}}\|} \leq 0.0001$
8. If condition 6 is not fulfilled, return to 1 with $i \leftarrow i+1$.

with

$$\boldsymbol{R}^i_{Ii} = \int_\Omega N_I\,\rho_{f,s}N_J d\Omega\;\bar{\dot{v}}^i_{Ji} + \int_\Omega \frac{\partial N_I}{\partial x_j}\sigma^i_{ij}d\Omega - \int_\Omega N_I{}^{n+1}b_i d\Omega$$

$$\boldsymbol{K}^m_{IJ} = \int_\Omega \boldsymbol{B}^T_I \Delta t c_{f,s}\boldsymbol{B}_J d\Omega,\;\; \boldsymbol{K}^\rho_{IJ} = \boldsymbol{I}\int_\Omega N_I\frac{2\rho_{f,s}}{\Delta t}N_J d\Omega$$

$$M_{1_{IJ}} = \int_\Omega \frac{1}{\kappa_{f,s}}N_I N_J d\Omega,\;\; M_{2_{IJ}} = \int_\Omega \tau\frac{\rho_f}{\kappa_f}N_I N_J d\Omega,\;\; \tau = \left(\frac{8\mu}{h^2} + \frac{2\rho_f}{\delta}\right)^{-1}$$

$$L_{IJ} = \int_\Omega \tau(\boldsymbol{\nabla}^T N_I)\boldsymbol{\nabla}N_J d\Omega,\;\; M_{b_{IJ}} = \int_{\Gamma_t}\frac{2\pi}{h_n}N_I N_J d\Gamma,$$

$$\mathbf{Q}_{IJ} = \int_\Omega \mathbf{B}^T_I\mathbf{m}N_J d\Omega$$

$$f_{p_I} = \int_{\Gamma_t}\tau N_I\left[\rho_f\frac{D\bar{v}_n}{Dt} - \frac{2}{h_n}(2\mu d_n - t_n)\right]d\Gamma - \int_\Omega \tau\boldsymbol{\nabla}^T N_I\boldsymbol{b}d\Omega$$

where N_I are the linear shape functions and h and δ are characteristic distances in space and time [49], and for 3D problems:

$$\boldsymbol{c}_f = \begin{bmatrix} \kappa_f + \frac{4\mu}{3\Delta t} & \kappa_f - \frac{2\mu}{3\Delta t} & \kappa_f - \frac{2\mu\Delta t}{3} & 0 & 0 & 0 \\ \kappa_f - \frac{2\mu\Delta t}{3} & \kappa_f + \frac{4\mu}{3\Delta t} & \kappa_f - \frac{2\mu}{3\Delta t} & 0 & 0 & 0 \\ \kappa_f - \frac{2\mu}{3\Delta t} & \kappa_f - \frac{2\mu}{3\Delta t} & \kappa_f + \frac{4\mu}{3\Delta t} & 0 & 0 & 0 \\ 0 & 0 & 0 & \frac{\mu}{\Delta t} & 0 & 0 \\ 0 & 0 & 0 & 0 & \frac{\mu}{\Delta t} & 0 \\ 0 & 0 & 0 & 0 & 0 & \frac{\mu}{\Delta t} \end{bmatrix}$$

$$\boldsymbol{c}_s = \begin{bmatrix} \kappa_s + \frac{4G}{3} & \kappa_s - \frac{2G}{3} & \kappa_s - \frac{2G}{3} & 0 & 0 & 0 \\ \kappa_s - \frac{2G}{3} & \kappa_s + \frac{4G}{3} & \kappa_s - \frac{2G}{3} & 0 & 0 & 0 \\ \kappa_s - \frac{2G}{3} & \kappa_s - \frac{2G}{3} & \kappa_s + \frac{4G}{3} & 0 & 0 & 0 \\ 0 & 0 & 0 & G & 0 & 0 \\ 0 & 0 & 0 & 0 & G & 0 \\ 0 & 0 & 0 & 0 & 0 & G \end{bmatrix}$$

$$\mathbf{B}_I = \begin{bmatrix} \frac{\partial N_I}{\partial x} & 0 & 0 \\ 0 & \frac{\partial N_I}{\partial y} & 0 \\ 0 & 0 & \frac{\partial N_I}{\partial z} \\ \frac{\partial N_I}{\partial y} & \frac{\partial N_I}{\partial x} & 0 \\ \frac{\partial N_I}{\partial z} & 0 & \frac{\partial N_I}{\partial x} \\ 0 & \frac{\partial N_I}{\partial z} & \frac{\partial N_I}{\partial y} \end{bmatrix},\;\; \boldsymbol{m} = \begin{bmatrix} 1 \\ 1 \\ 1 \\ 0 \\ 0 \\ 0 \end{bmatrix}$$

References

[1] S. Abdali, E. Mitsoulis, N. Markatos, Entry and exit flows of bingham fluids, J. Rheol. 36 (2) (1992) 389–407.
[2] C. Ancey, Plasticity and geophysical flows: a review, J. Nonnew. Fluid Mech. 142 (2007) 4–35.
[3] S. Andersen, L. Andersen, Modelling of landslides with the material-point method, Comput. Geosci. 14 (1) (2010) 137–147.
[4] P. Becker, S.R. Idelsohn, E. Oñate, A unified monolithic approach for multi-fluid flows and fluid-structure interaction using the particle finite element method with fixed mesh, Comput. Mech. 61 (2015) 1–14.

[5] P.A. Becker, S.R. Idelsohn, A multiresolution strategy for solving landslides using the particle finite element method, Acta Geotech. 11 (3) (2016) 643–657.
[6] T. Belytschko, W.K. Liu, B. Moran, K.I. Elkhodadry, Nonlinear Finite Elements For Continua And Structures, 2nd, John Wiley & Sons, New York, 2014.
[7] M. Bercovier, M. Engelman, A finite-element method for incompressible non-newtonian flows, J. Comput. Phys. 36 (3) (1980) 313–326.
[8] E.C. Bingham, Fluidity and Plasticity, McGraw-Hill, New York, 1922.
[9] E. Bovet, B. Chiaia, L. Preziosi, A new model for snow avalanche dynamics based on non-newtonian fluids, Meccanica 45 (6) (2010) 753–765.
[10] F. Brezzi, M. Fortin, Mixed And Hybrid Finite Element Methods, Springer, New York, 1991.
[11] A. Designation, Standard test method for slump of hydraulic cement concrete, in: Annual Book of ASTM Standards, 04 01, 1996, pp. 85–87. C-143-90
[12] A. Designation, Standard specification for flow table for use in tests of hydraulic cement, Annual Book of ASTM Standards, 04 01, 2004. C230/C230M-03
[13] H. Chanson, S. Jarny, P. Coussot, Dam break wave of thixotropic fluid, J. Hydraul. Eng. 123 (3) (2006) 280–293.
[14] M. Cremonesi, L. Ferrara, A. Frangi, U. Perego, Simulation of the flow of fresh cement suspensions by a lagrangian finite element approach, J. Nonnewton. Fluid Mech. 165 (2010) 1555–1563.
[15] M. Cremonesi, F. Ferri, U. Perego, A basal slip model for lagrangian finite element simulations of 3d landslides, Int. J. Numer. Anal. Methods Geomech. 41 (2017) 30–53.
[16] M. Cremonesi, A. Frangi, U. Perego, A lagrangian finite element approach for the simulation of water-waves induced by landslides, Comput. Struct. 89 (2011) 1086–1093.
[17] Z. Dai, Y. Huang, H. Cheng, Q. Xu, Sph model for fluid–structure interaction and its application to debris flow impact estimation, Landslides 14 (3) (2017) 917–928.
[18] J.D. Dent, T.E. Lang, A biviscous modified bingham model of snow avalanche motion, Ann. Glaciol. 4 (1983) 42–46.
[19] H. Edelsbrunner, E.P. Mucke, Three dimensional alpha shapes, ACM Trans. Graphics 13 (1999) 43–72.
[20] H. Edelsbrunner, T.S. Tan, An upper bound for conforming delaunay triangulations, Discrete Comput. Geo. 10 (2) (1993) 197:213.
[21] M. Fortin, R. Glowinski, Augmented Lagrangian Methods, Elsevier, Amsterdam, 1983.
[22] A. Franci, M. Cremonesi, On the effect of standard pfem remeshing on volume conservation in free-surface fluid flow problems, Comput. Particle Mech. 4 (3) (2017) 331–343.
[23] A. Franci, E. Oñate, J.M. Carbonell, Unified lagrangian formulation for solid and fluid mechanics and fsi problems, Comput. Methods Appl. Mech. Eng. 298 (2016) 520–547.
[24] A. Franci, E. Oñate, J.M. Carbonell, Velocity-based formulations for standard and quasi-incompressible hypoelastic-plastic solids, Int. J. Numer. Methods Eng. 107 (11) (2016) 970–990.
[25] W.H. Herschel, R. Bulkley, Konsistenzmessungen von gummi-benzollösungen, Kolloid-Zeitschrift 39 (4) (1926) 291–300.
[26] S.M. Hosseini, M.T. Manzari, S.K. Hannani, A fully explicit three-step sph algorithm for simulation of non-newtonian fluid flow, Int. J. Numer. Methods Heat Fluid Flow 17 (7) (2007) 715–735.
[27] B. Hubner, E. Walhorn, D. Dinkler, A monolithic approach to fluid-structure interaction using space-time finite elements, Comput. Methods Appl. Mech. Eng. 193 (2004) 2087–2104.
[28] S.R. Idelsohn, J. Marti, A. Limache, E. Oñate, Unified lagrangian formulation for elastic solids and incompressible fluids: applications to fluid-structure interaction problems via the pfem, Comput. Methods Appl. Mech. Eng. 197 (2008) 1762–1776.
[29] S.R. Idelsohn, E. Oñate, F.D. Pin., The particle finite element method: a powerful tool to solve incompressible flows with free-surfaces and breaking waves, Int. J. Numer. Methods Eng. 61 (2004) 964–989.
[30] R.M. Iverson, The physics of debris flows, Rev. Geophys. 35 (3) (1997) 245–296.
[31] J.S.H. Kwan, Development of numerical models for landslide mitigation works, JTC1 Workshop on Advances in Landslides Understanding, Barcelona, Spain, 2017.
[32] A. Larese, A lagrangian pfem approach for non-newtonian viscoplastic materials, Revista Internacional De Metodos Numericos para Calculo y Diseño en Ingenieria 33 (3–4) (2017) 307–317.
[33] A. Leonardi, F.K. Wittel, M. Mendoza, Lattice-boltzmann method for geophysical plastic flows, in: W. Wu (Ed.), Recent Advances in Modeling Landslides and Debris Flows, Springer Series in Geomechanics and Geoengineering, Springer, Cham, 2015.
[34] A. Leonardi, F.K. Wittel, M. Mendoza, H.J. Herrmann, Coupled dem-lbm method for the free-surface simulation of heterogeneous suspensions, Comput. Particle Mech. 1 (2014) 3–13.
[35] A. Leonardi, F.K. Wittel, M. Mendoza, R. Vetter, H.J. Herrmann, Particle-fluid-structure interaction for debris flow impact on flexible barriers, Comput.-Aided Civ. Infrastruct. Eng. 0 (2015) 1–11.
[36] K.F. Liu, C.C. Mei, Slow spreading of a sheet of bingham fluid on an inclined plane, J. Fluid Mech. 207 (1989) 505–529.
[37] Y. Liu, N. Balmforth, S. Hormozi, D. Hewitt, Two-dimensional viscoplastic dambreaks, J. Nonnewton. Fluid Mech. 238 (2016) 65–79.
[38] L. Lucy, A numerical approach to the testing of the fission hypothesis, Astronom. J. 82 (1977) 1013–1024.
[39] M. Manga, M. Bonini, Large historical eruptions at subaerial mud volcanoes, italy, Nat. Hazards Earth Syst. Sci. 12 (2012) 3377–3386.
[40] S.M. Dougall, O. Hungr, A model for the analysis of rapid landslide motion across three-dimensional terrain, Can. Geotechnical J. 41 (6) (2004) 1084–1097.
[41] S. Meduri, M. Cremonesi, U. Perego, O. Bettinotti, A. Kurkchubasche, V.M. Oancea., A partitioned fully explicit lagrangian finite element method for highly nonlinear fluid-structure interaction problems, Int. J. Numer. Methods Eng. 113 (2018) 43–64.
[42] L. Minatti, A. Pasculli, Sph numerical approach in modelling 2d muddy debris flow, in: International Conference on Debris-Flow Hazards Mitigation: Mechanics, Prediction, and Assessment, 2011, pp. 467–475.
[43] E. Mitsoulis, T. Zisis, Flow of bingham plastics in a lid-driven square cavity, J. Nonnewton. Fluid Mech. 101 (2001) 173–180.
[44] E. Moreno, A. Larese, M. Cervera, Modelling of bingham and herschel-bulkley flow with mixed p1/p1 finite elements stabilized with orthogonal subgrid scale, J. Nonnewton. Fluid Mech. 228 (2016) 1–16.
[45] L. Muravleva, E. Muravleva, G.C. Georgiou, E. Mitsoulis, Numerical simulations of cessation flows of a bingham plastic with the augmented lagrangian method, J. Nonnewton. Fluid Mech. 165 (2010) 544–550.
[46] C.W.W. Ng, C.E. Choi, D. Song, A particle method for history-dependent materials, JTC1 Workshop on Advances in Landslides Understanding, 2017. Barcelona, Spain
[47] X. Oliver, J.C. Cante, R. Weyler, C. González, J. Hernández, Particle finite element methods in solid mechanics problems, in: E. Oñate, R. Owen (Eds.), Computational Plasticity, Springer, Berlin, 2007.
[48] E. Oñate, M.A. Celigueta, S.R. Idelsohn, F. Salazar, B. Suarez, Possibilities of the particle finite element method for fluid-soil-structure interaction problems, Comput. Mech. 48 (2011) 307–318.
[49] E. Oñate, A. Franci, J.M. Carbonell, Lagrangian formulation for finite element analysis of quasi-incompressible fluids with reduced mass losses, Int. J. Numer. Methods Fluids 74 (10) (2014) 699–731.
[50] E. Oñate, S.R. Idelsohn, F.D. Pin, R. Aubry, The particle finite element method. an overview, Int. J. Comput. Methods 1 (2004) 267–307.
[51] E. Oñate, J. Marti, R. Rossi, S.R. Idelsohn, Analysis of the melting, burning and flame spread of polymers with the particle finite element method, Comput. Assist. Methods Eng. Sci. 20 (2013) 165–184.
[52] T.C. Papanastasiou, Flows of materials with yield, J. Rheol. 31 (1987) 385–404.
[53] J.D. Parsons, K.X. Whipple, A. Simoni, Experimental study of the grain flow, fluid–mud transition in debris flows, J. Geol. 109 (4) (2001) 427–447.
[54] M. Pastor, T. Blanc, B. Haddad, V. Drempetic, M.S. Morles, P. Dutto, M.M. Stickle, P. Mira, J.A.F. Merodo, Depth averaged models for fast landslide propagation: mathematical, rheological and numerical aspects, Arch. Comput. Methods Eng. 22 (1) (2015) 67–104.
[55] N.M. Pinyol, M. Alvarado, E.E. Alonso, F. Zabala, Thermal effects in landslide mobility, Géotechnique (2017) 1–18.
[56] M.J.D. Powell, A Method for Nonlinear Constraints in Minimization Problems, Academic Press, New York, 1969.
[57] A. Remaître, J.P. Malet, O. Maquaire, C. Ancey, J. Locat, Flow behaviour and runout modelling of a complex debris flow in a clay-shale basin, Earth Surf. Processes Landforms 30 (4) (2005) 479–488.
[58] N. Roussel, P. Coussot, Fifty-cent rheometer for yield stress measurements: from slump to spreading flow, J.Rheol. 49 (3) (2005) 705–718.
[59] N. Roussel, M.R. Geiker, F. Dufour, L.N. Thrane, P. Szabo, Computational modeling of concrete flow: general overview, Cem. Concr. Res. 37 (9) (2007) 1298–1307.
[60] P. Ryzhakov, E. Oñate, S.R. Idelsohn, Improving mass conservation in simulation of incompressible flows, Int. J. Numer. Methods Eng. 90 (2012) 1435–1451.
[61] F. Salazar, J. Irazabal, A. Larese, E. Oñate, Numerical modelling of landslide-generated waves with the particle finite element method (pfem) and a non-newtonian flow model, Int. J. Numer. Anal. Methods Geomech. 40 (2016) 809–826.
[62] P. Saramito, A. Wachs, Progress in numerical simulation of yield stress fluid flows, Rheol. Acta 56 (3) (2017) 211–230.
[63] S. Shao, E.Y.M. Lo, Incompressible sph method for simulating newtonian and non-newtonian flows with free surface, Adv. Water Resour. 26 (2003) 787–800.
[64] H.P. Soto, M.L. Martins-Costa, C. Fonseca, S. Frey, A numerical investigation of inertia flows of bingham-papanastasiou fluids by an extra stress-pressure velocity galerkin least-squares method, J. Brazilian Soc. Mech. Sci. Eng. 32 (5) (2010) 450–460.
[65] S. Succi, The Lattice Boltzmann Equation for Fluid Dynamics and Beyond, Oxford University Press, New York, 2001.
[66] D. Sulsky, Z. Chen, H. Schreyer, A particle method for history-dependent materials, Comput. Methods Appl. Mech. Eng. 118 (1994) 179–196.
[67] L.N. Thrane, C. Pade, C.V. Nielsen, Determination of rheology of self-consolidating concrete using the 4c-rheometer and how to make use of the results, J. ASTM Int. 7 (2010) 1–10.
[68] K.X. Whipple, Open channel flow of bingham fluids: applications in debris flow research, J. Geol. 105 (2) (1997) 243–262.
[69] X. Zhang, K. Krabbenhoft, D. Sheng, Particle finite element analysis of the granular column collapse problem, Granular Matter 16 (2014) 609–619.
[70] X. Zhang, D. Sheng, S.W. Sloan, J. Bleyer, Lagrangian modelling of large deformation induced by progressive failure of sensitive clays with elastoviscoplasticity, Int. J. Numer. Methods Eng. 112 (2017) 963–989.
[71] M. Zhu, M.H. Scott, Modeling fluid-structure interaction by the particle finite element method in opensees, Comput. Struct. 132 (2014) 12–21.
[72] O.C. Zienkiewicz, R.L. Taylor, The finite element method, Its Basis and Fundamentals, sixth ed., Elsevier Butterworth-Heinemann, Oxford, 2005.